In-situ synchrotron X-ray diffraction investigation of martensite decomposition in Laser Powder Bed Fusion (L-PBF) processed Ti-6Al-4V

Pushkar Prakash Dhekne[1,2*], Matthias Bönisch[1], Marc Seefeldt[1], Kim Vanmeensel[1*]

[1]*KU Leuven, Department of Materials Engineering, Kasteelpark Arenberg 44 box 2450, B-3001 Heverlee, Belgium*
[2]*SIM M3 program, Technologiepark 48, B-9052 Zwijnaarde, Belgium*

Abstract

Laser powder bed fusion (L-PBF) processed Ti-6Al-4V components present two substantial challenges: the presence of tensile residual stress and brittleness of the as-fabricated component due to the formation of the martensite (α′) phase. Industrially, post-heat treatment is performed to improve the quasi-static mechanical properties of the Ti-6Al-4V component through martensite (α′) decomposition and residual stress relaxation. However, detailed insights into the martensite decomposition and stress relaxation mechanisms are still lacking. To address this, in-situ high-energy synchrotron x-ray diffraction (HEXRD) was employed to simultaneously track: (I) martensite (α′) decomposition into a mixture of hexagonal α and body-centered cubic β phases, (II) residual stress relaxation process during heating. Rietveld refinement of 2D diffraction patterns recorded over a temperature range spanning from 25 to 1000°C revealed a three-stage evolution in the α′ unit cell parameters. Unit cell parameter analysis combined with the phase fraction analysis based on the diffraction patterns and the chemical composition profiles predicted by Thermocalc simulation gave detailed insight into the martensite (α′) decomposition process. In Stage 1 (until 375°C), the α′ phase unit cell exhibited linear expansion without indications of any phase transformation or stress relaxation. Upon commencement of stage II at 375°C, an increased expansion rate of the martensite (α′) unit cell was observed, attributed to the enhanced outward diffusion of vanadium (V), succeeded by β phase nucleation at 575°C. Simultaneously, during stage II, residual stress relaxation was observed at both macro and micro scale, culminating in a stress-free state achieved at approximately 750-800°C. Lastly, α-to-β phase transformation was observed in stage 3. The thermal evolution of the hexagonal unit cell dimensions was compared between martensitic and mill-annealed α+β microstructures. This comparison unraveled the link between the initial microstructure and the thermal expansion behavior of the hexagonal α′ and α phase.

Introduction

Laser Powder Bed Fusion (L-PBF) is an additive manufacturing (AM) technique involving the selective melting of a powder bed with a high-power laser [1]. The main advantage of L-PBF processing lies in its ability and relative ease of manufacturing complex-shaped parts compared to traditional manufacturing techniques [2]. The complex-shaped Ti-6Al-4V parts have a huge application potential in the bio-medical and aerospace industries. However, the exceptionally high cooling rates experienced during L-PBF processing induce tensile residual stresses as well and trigger a diffusion-less β (body-centered cubic, BCC) phase to the hexagonal (HCP) martensite (α′) phase transformation. Both of these factors result in a lower tensile elongation of ~4-7% in the as-fabricated Ti-6Al-4V component [3,4]. Thus, the decomposition of α′ phase and relaxation of residual stresses is key to enhancing the quasi-static mechanical properties of L-PBF processed Ti-6Al-4V.

Industrially, a stress-relieving post-heat treatment is performed to (I) Decompose the metastable α′ phase into a mixture consisting of the Al-rich α (HCP) and the V-rich β (BCC) phases and (II) Alleviate the tensile residual stresses. Another approach to achieve the two objectives is by altering the thermal history of the component during the L-PBF processing in a way that the part is maintained

at a high temperature for a sufficiently long time, which slows down the cooling rate, further resulting in the α′ decomposition and residual stress relaxation [5]. Some of the common strategies to achieve in-situ α′ decomposition are: applying higher laser energy density during L-PBF, using laser rescanning strategies, or preheating the build plates [5,6]. Moreover, enhanced tensile elongation in an as-built component has been achieved using the aforementioned in-situ approaches [7–9]. However, higher laser energy densities and rescanning strategies decrease the L-PBF productivity, while baseplate preheating could lead to decreased product quality due to increased oxygen pick-up, making these approaches less attractive for industries [10]. As such, stress-relieving annealing is the most viable option to decompose the α′ microstructure and relax the residual stresses in an L-PBF processed Ti-6Al-4V component.

A plethora of literature exists on the influence of different stress relieving heat treatments on the microstructure, mechanical properties, and residual stress state [11–14]. Previously, ex-situ characterization has been applied to study martensite decomposition, which does not capture certain aspects such as the β nucleation temperature, temperature of initiation, and completion of α′ decomposition. [14,15]. The bridging of this knowledge gap requires real-time tracking of the α′ decomposition during heating, which has garnered less attention. Kaschel et al. monitored the α′ decomposition by in-situ lab-scale x-ray diffraction (XRD) [16]. However, due to its limited penetration depth, lab-scale XRD can only probe the volume near the surface, which might not fully represent the bulk specimen [17]. Another disadvantage of lab-scale XRD is its low detection limit (2 mass%), which limits the accurate detection of certain phenomena such as β phase nucleation [18]. To address these limitations, Lakroune et al. and Brown et al. employed high-energy synchrotron diffraction (HEXRD) through which phase transformations can be tracked accurately by probing a volume order of magnitude larger than the one probed by lab scale XRD[19,20]. However, their analysis lacked the link between the compositional change of the α′ phase and the evolution of the lattice parameters of the hexagonal α′ unit cell. Moreover, the latter report did not integrate the simultaneous residual stress evolution during the solid-state phase transformation.

Therefore, the current investigation aims to understand: (A1) the process of α′ decomposition during continuous heating and (A2) the evolution of the residual stress state with temperature. Aim (A1) was achieved by performing dilatometry coupled with in-situ synchrotron high energy X-ray diffraction (HEXRD). Firstly, the evolution of the unit cell parameters of α′ and β phases was monitored through in-situ HEXRD during heating. Secondly, in-situ dilatometry was performed to track phase transformations during heating. Furthermore, Thermocalc software employing the CALPHAD method (Calculation of Phase Diagrams) was used to relate the change in chemical composition of both the α and β phases to the evolution of their respective lattice parameters. Aim (A2) was achieved by (i) evaluating the macroscopic residual stress state as a function of temperature and by (ii) tracking the evolution of the full width at half maximum (FWHM) of the diffraction peaks to monitor the micro-scale residual stresses. Finally, the thermal expansion behavior of martensite (α′) and mill-annealed (α+β) Ti-6Al-4V during continuous heating is compared.

2. Materials and Methods

2.1. L-PBF processing

Cubic Ti-6Al-4V specimens with a volume of 10 mm^3 were manufactured on a ProX320 machine in protective Ar environment. L-PBF parameters employed are listed in Table 1.

Table 1: L-PBF parameters

Parameter	Value
Laser power (W)	90

Scan velocity (mm/s)	1000
Layer thickness (μm)	30
Hatch spacing (μm)	90
Scan rotation (°)	90

Figure 1 presents the initial martensitic microstructure obtained after the L-PBF processing.

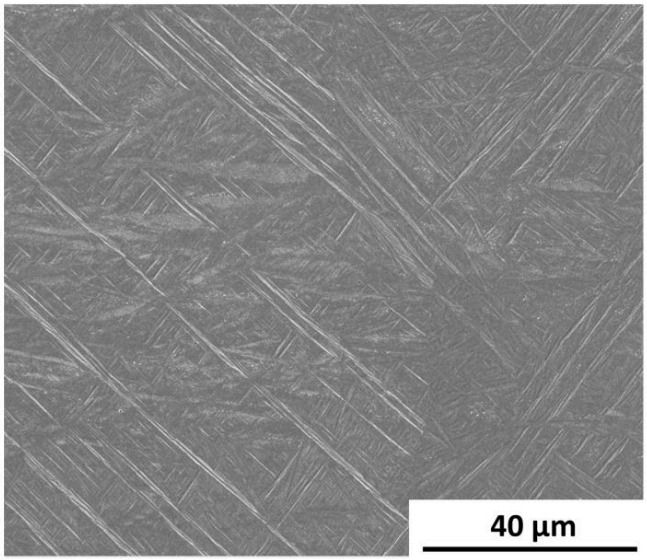

Figure 1: Initial martensitic microstructure

2.2. Synchrotron high-energy X-ray diffraction

In-situ synchrotron high energy X-ray diffraction (HEXRD) during heat treatment was performed at DESY on the PETRA III P07 beamline. A schematic diagram of the experimental setup is shown in Figure 2 (A). 2D Diffraction patterns (see Figure 2 (B)) were recorded in transmission mode on a 2D Perkin Elmers detector containing 2048 X 2048 pixels, with each pixel being a square of 200 X 200 μm^2. To measure thermal strain, the sample was clamped horizontally between two quartz rods inside a modified Bähr DIL 805 A/D dilatometer from TA instruments. The sample was heated inductively from room temperature to 1050°C at 20°C/min in a vacuum (10^{-5} mbar) environment, and a diffraction pattern was recorded every 2s with a 100 keV synchrotron X-ray beam and a spot size of 0.8 x 0.8 mm^2. Sample temperature was measured using a type S thermocouple welded to the sample's surface.

2.3. Analysis of diffraction patterns

Firstly, a LaB_6 reference diffraction pattern was processed with Fit2d software to accurately determine the coordinates of the beam center, the angular tilt of the detector, the instrumental broadening and the sample-to-detector distance [21]. Later, 2D diffraction patterns obtained during heating were azimuthally caked into 36 slices of 10°. Each of the 36 slices were integrated into a 1D pattern (intensity vs 2θ) and combined into one file, that was used for Rietveld refinement in MAUD [22]. For Rietveld refinement, the Delft type line broadening [23] and isotropic size-strain models were used. The E-WIMV texture model was used to account for the crystallographic texture [24]. The triaxial isotropic stress model was employed to obtain the deviatoric residual stress. The model

calculates deviatoric stresses by assuming isotropic Young's modulus (116 GPa) and Poisson's ratio (0.3). To obtain a unique values for deviatoric stress, the normal deviatoric stress components in the detector plane (σ_{11}, σ_{33}) were constrained to each other by $\sigma_{11} = -\sigma_{33}$. Appendix A explains the motivation behind this constraint.

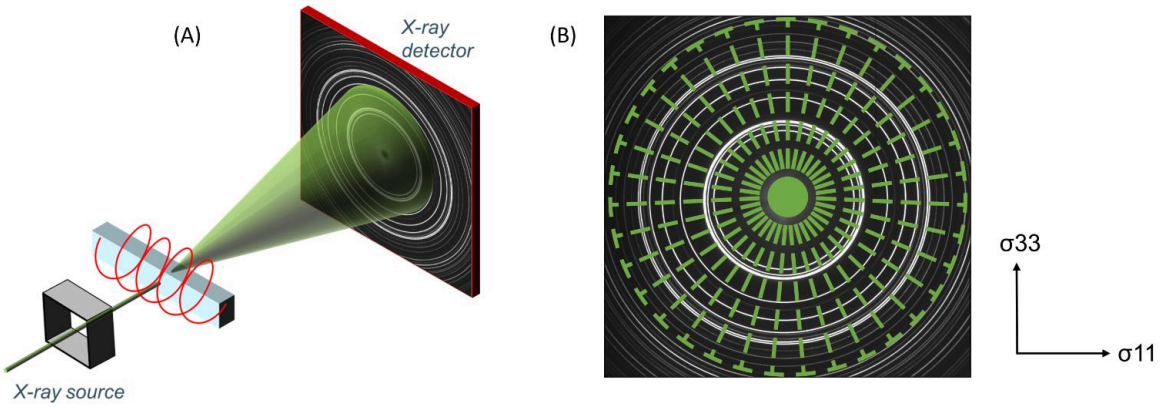

Figure 2: (A) Schematic depiction of the in-situ heating setup at the DESY P07 beamline. (B) 2D diffraction pattern obtained during in-situ synchrotron diffraction experiment. Green sectors show the 36 slices of 10°.

2.4. Thermodynamic Simulation

Theoretical Al and V composition of α and β phase were calculated using Thermo-Calc 2022a software with TCTI2: Ti-Alloys v2.2 and MOBTI3 as thermodynamic and kinetic database, respectively. The simulations were performed with the standard pressure of 100000 Pa (1 bar) on a system size of 1 mol.

3. Results

3.1. In-situ Dilatometry

In-situ dilatometry was performed to track the solid-state phase transformations during heating. The evolution of the macroscopic strain obtained during continuous heating is shown in Figure 3 (A-C). Initially, the macroscopic strain increases at a constant rate till 450°C, followed by the lower strain increment rate between 450°C to 650°C (see the magnified plot in Figure 3 (B)). The slowed strain increment is better visualized in the derivative of the dilatometric curve, represented by the blue curve in Figure 3 (B). To relate the slope change of the dilatometric curve with a phase transformation, smaller sections of the diffraction patterns (2θ ranging from 2.9°-3.3°) corresponding to 200°C, 400°C, 600°C, 800°C and 1000°C are shown in Figure 3 (D-H). Initially, at 200°C and 400°C, only α′ reflections are present without any signs of the β phase. β phase reflections are only observed after heating above 575°C. The observed slope change of the dilatometric curve between 450°C and 650°C can potentially be linked to the nucleation of the β phase. Upon further heating, an even greater change in the slope of the dilatometric curve is observed above 750°C. In the same temperature range, β phase reflections intensify at the expense of the weakened α phase reflections (see Figure 3 (G, H). Thus, the second deviation in the dilatometric curve can be attributed to the α-to-β solid-state phase transformation. In summary, the dilatometric analysis indicates two phase transformations occurring during heating, namely the nucleation of the β phase between 450°C-650°C and the gradual α-to-β phase transformation from 750°C to β transus temperature.

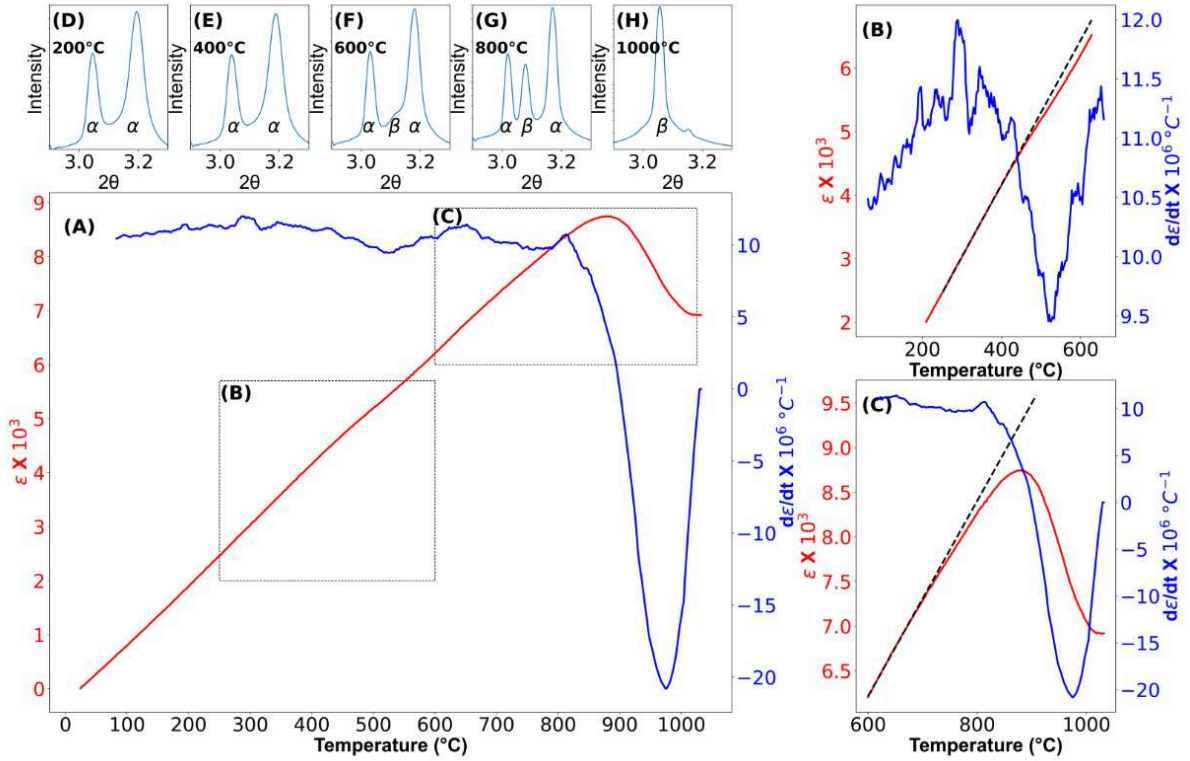

Figure 3: (A) Evolution of the macroscopic strain during in-situ dilatometry. Zoomed-in plot to highlight: (B) deviation from linearity at 450°C, indicating the initiation of α′ decomposition and (C) deviation from linearity due to α-β allotropic phase transformation. Black dashed lines in (B) and (C) indicate linear regression curves fitted for initial 30 data points to highlight the change of slope of the dilatometric curve. The diffraction patterns corresponding to (D) 200°C (E) 400°C (F) 600°C (G) 800°C (H) 1000°C are presented to link the slope change in the dilatometric curve to phase transformations.

3.2. Heating with in-situ high energy x-ray diffraction (HEXRD)

Real-time α′ decomposition was monitored by the HEXRD during continuous heating. Figure 4 (A) presents 1D diffraction patterns obtained by integrating the 2D diffraction over the complete azimuthal range of 360° at different temperatures. At room temperature, only diffraction peaks corresponding to the hexagonal α′ phase were observed without any sign of the β phase. Similar observations have been made for as-fabricated Ti-6Al-4V components [19,20,25]. Upon gradual heating, α′ diffraction peaks shift to lower diffraction angles, indicating the expansion of the α′ unit cell. The first reflection of the β phase is observed at 575°C, evidenced by the appearance of a shoulder on the {10.1} peak, marking the initiation of α′ decomposition. Since the β phase is rich in V content, its nucleation would cause V depletion in the neighboring α′ lath, suggesting the presence of V-rich and V-lean α′ regions. However, no peak splitting was observed for the α′ reflections at temperatures above 575°C, which might have risen due to the presence of two different types of α′ phase. This was confirmed by quantifying the peak asymmetry by fitting the α′ reflections with the split pseudo Voigt function (indicated in Appendix B). However, the absence of a clear trend in peak asymmetry evolution contrasts Kaschel et al., who reported peak splitting of $\{00.2\}_{\alpha'}$ reflection, recorded on a lab-scale XRD, during α′ decomposition [16]. Upon heating above 700°C, gradual α-to-β phase transformation causes the intensification of the $\{110\}_{\beta}$ reflection along with the formation of new $\{200\}_{\beta}$ and $\{211\}_{\beta}$ reflections at 4.38° and 5.36°, respectively, also reflected by the change of slope in the dilatometric curve above 700°C. Finally, α-to-β phase transformation completes at

1005°C. Appendix C shows the evolution of the phase fraction of α/α′ and β as a function of temperature.

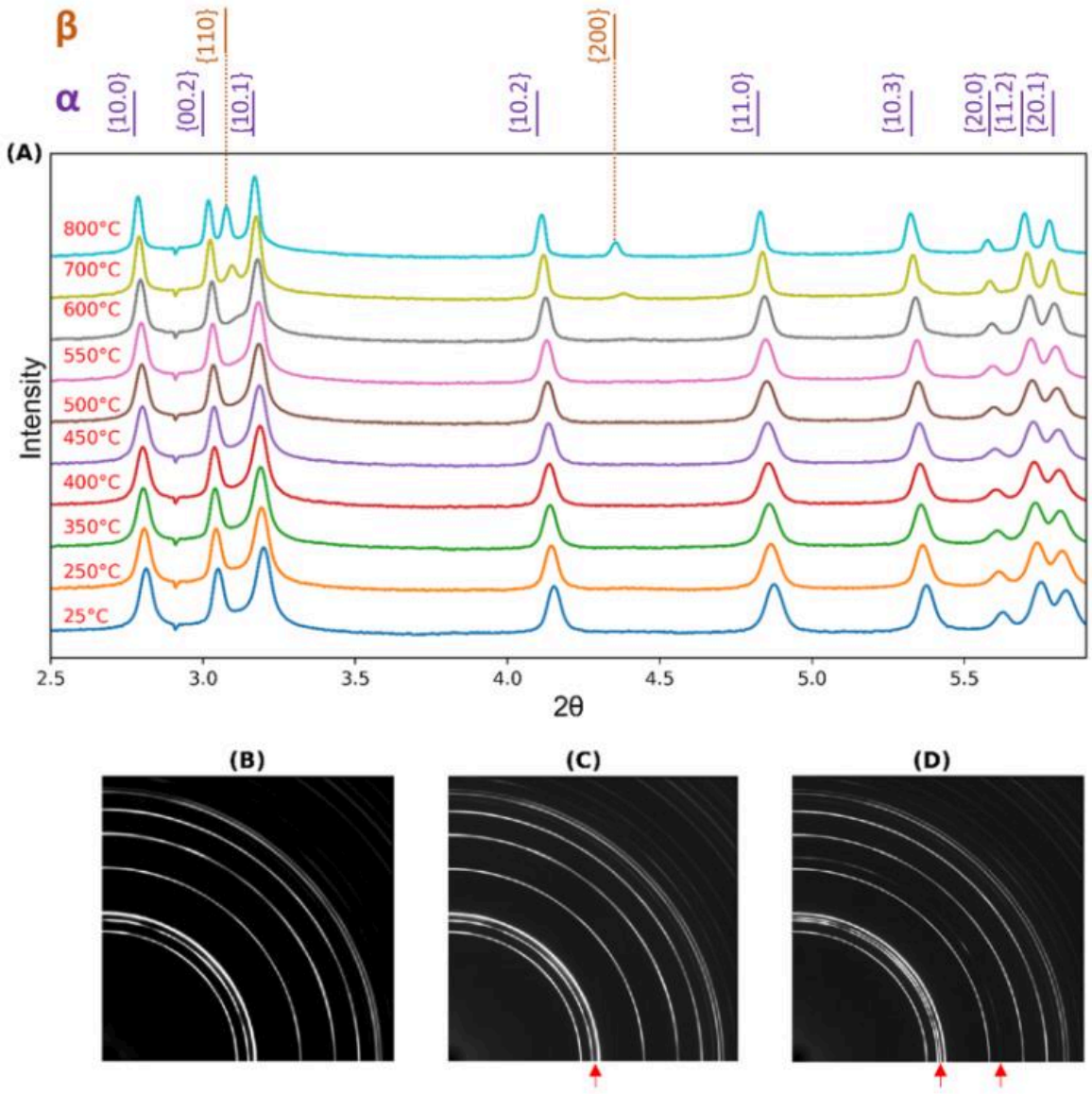

Figure 4: (A) 1-D diffraction patterns obtained after complete azimuthal integration of 2D diffraction patterns recorded at different temperatures (the small dimple at 2.9° is due to the presence of dead pixels on the detector). 2D diffraction pattern recorded at (B) 25°C, (C) 600°C and (D) 800°C. Red arrows in (C) and (D) points the location of the β phase diffraction ring.

3.3. In-situ lattice parameter monitoring

The evolution of the α′ unit cell dimensions with temperature is shown in Figure 5 (A-G). The a and the c lattice parameters monotonically increase with temperature, albeit with a different slope in the different temperature ranges. The evolution of the lattice parameters can be subdivided into three stages, indicated in Figure 5 (A & B). Figure 5 (D, F) presents the magnified view of Figure 5 (A) in the temperature range of 100-500°C and 600-900°C, respectively, highlighting the different stages in the expansion of the a lattice parameter. The initial stage lasts until 375°C, during which the hexagonal α′ unit cell expands from 2.918 nm to 2.929 nm along the a-axis. The second stage is identified within 400 to 750°C temperature range, during which the α′ unit cell dimension increases

even more rapidly from 2.292 nm to 2.9433 nm along the a-direction. The last stage (750°C to the β transus temperature (~1005°C)) exhibits an even faster increase for the a lattice parameter. A similar three-staged evolution was observed for the c parameter of the α′ unit cell, shown in Figure 5 (B, F, G). Figure 5 (C) presents the c/a ratio evolution with temperature for the α′ unit cell. The ratio remains constant till 375°C as both the c and a parameter increase at a similar rate till 375°C. After 375°C, the α′ unit cell expands much more rapidly along the c-axis as compared to the a-axis, which results in the rapid increase in the c/a ratio of the α′ unit cell.

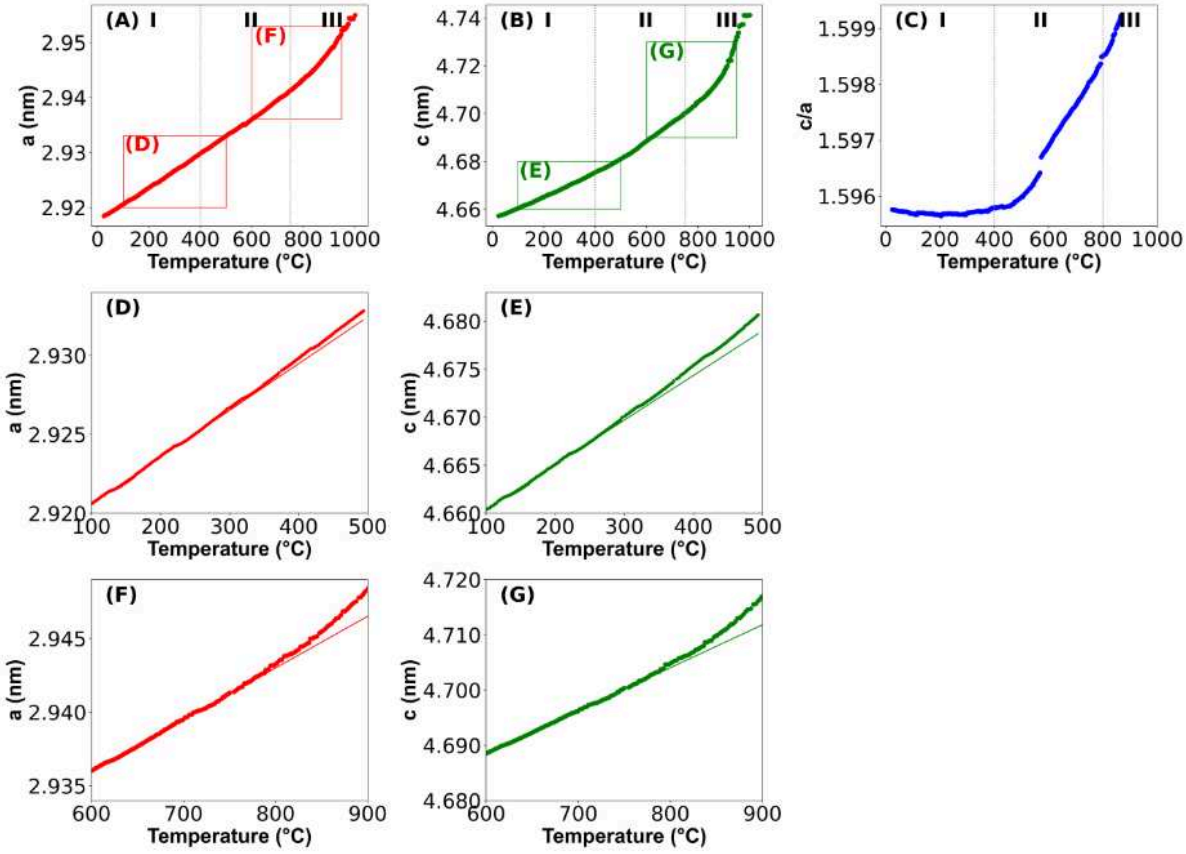

Figure 5: Thermal evolution of (A) a unit cell parameter, (B) c unit cell parameter and (C) c/a of α′ phase. (D, F) presents the zoomed version of (A) between 200–500°C and 600-1000°C for the a unit cell parameter. Similarly, (E, G) presents the zoomed version of (B) between 200–500°C and 600-1000°C for the a unit cell parameter.

Figure 6 shows the evolution of the β phase lattice parameter within the temperature range of 600°C - 1000°C. Although β phase reflections initially emerges at 575°C, the low intensities of β phase reflections hampered the assessment of the β phase unit cell parameter below 600°C. Accurate determination of the unit cell parameter was only possible above 600°C due to consistent intensification of the β phase reflections. The β phase unit cell parameter increases from 3.206 nm at 600°C to 3.288 nm at 1000°C. β phase unit cell parameter increases at a constant rate with temperature up to 775°C but unit cell expansion rate decreases at higher temperatures.

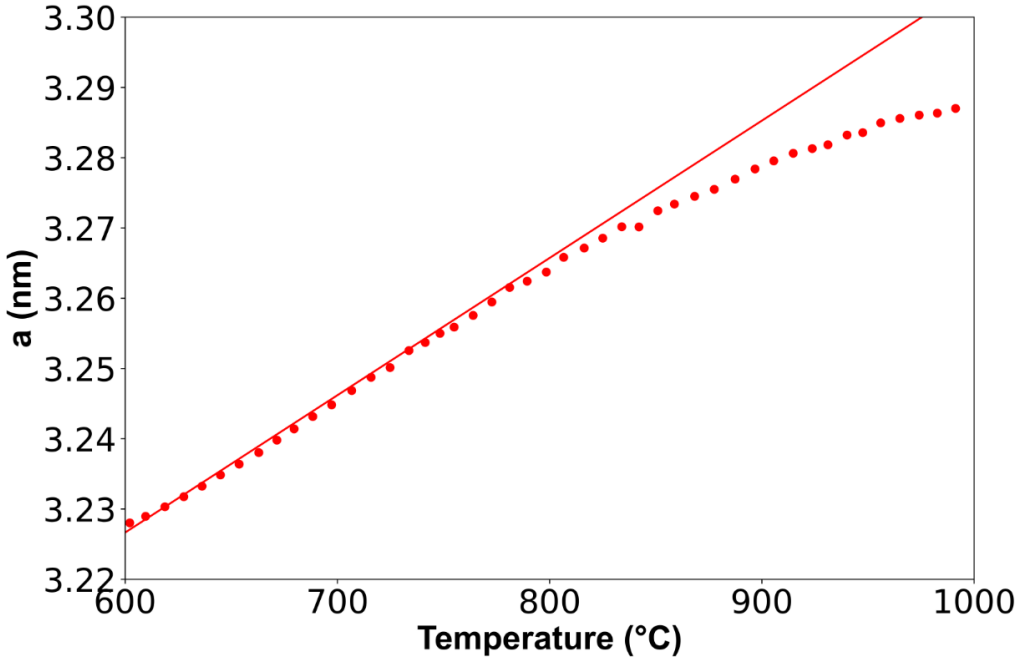

Figure 6: Evolution of the β phase lattice parameter during heating.

3.4. In-situ monitoring of residual stresses

HEXRD allows monitoring of the macroscopic (Type I) and microscopic (Type II + Type III) stresses during heating, in addition to the phase transformations. Here, the evolution of the deviatoric stress component along the building direction is used to track the evolution of the macroscopic residual stress relaxation process. Further motivation for this choice is discussed in Appendix D. Figure 7 (A) presents the evolution of the deviatoric residual stress during heating. The deviatoric residual stress remains constant upto 450°C, indicating no significant stress relaxation has commenced. At higher temperatures, the residual stress decreases constantly, and a stress-free state (stress ≈ 0) is reached around 750°C.

To quantify the evolution of the microscopic (Type III) stress state during heating, the evolution of the FWHM of α′ diffraction peak was tracked, as the FWHM is directly related to the defect density, which in-turn induces Type III residual stresses [26]. Figure 7 (B) presents the evolution of the FWHM of the {10.0}, {10.1}, {10.2}, {11.0}, and {10.3} reflections as a function of temperature. Values in Figure 7 (B) were obtained by averaging the FWHMs of the reflections across the 36 azimuthal sections. The FWHM evolution mirrors the trend of the macroscopic residual stress: it remains constant until 450°C, experiences a sudden drop in FWHM above 450°C, and plateaus at 750°C. Thus, the deviatoric stress component of the residual stress and the FWHM value evolution indicate complete relaxation of the macro and micro level residual stresses, respectively, at temperatures above 750°C.

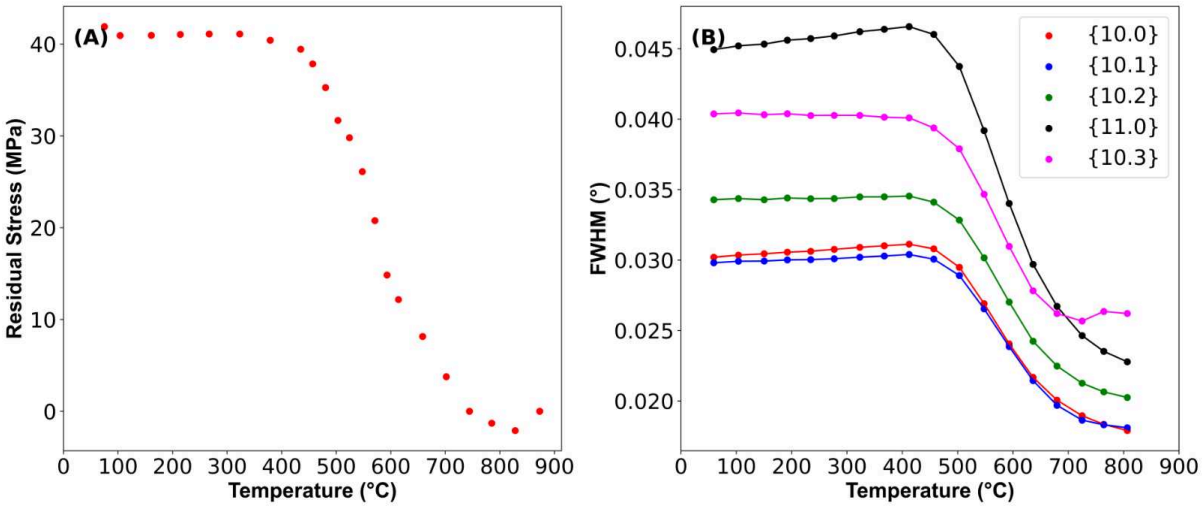

Figure 7: Evolution of (A) the deviatoric component of the macroscopic residual stress and (B) the full width half maximum (FWHM) of hexagonal α′ phase with temperature. The FWHM is indicative for the microscopic residual stress.

4. Discussion

4.1. Events occurring during martensite decomposition in Ti-6Al-4V

This section focuses on unraveling the complex phase transformation events during the heating of α′ phase. Three stages were identified based on the α′ unit cell parameter evolution as a function of temperature, as indicated in Figure 5 (A, B). The following paragraphs discuss the three stages (25-375°C, 375-750°C, and 750-1000°C) separately in detail.

Stage 1: Room Temperature to 375°C: : In this stage, both the a and c lattice parameters of the α′ phase unit cell linearly increase with temperature. The coefficient of thermal expansion (CTE), calculated from Figure 5 (D, E), suggests a faster expansion of the α′ phase unit cell along c-direction (10×10^{-6} °C^{-1}) than a-direction (9.2×10^{-6} °C^{-1}). Elmer et al. reported a similar CTE (9.2×10^{-6} °C^{-1}) for α phase along the a-direction for mill-annealed Ti-6Al-4V till 550°C, but did not report the expansion rate along the c-axis. Furthermore, Figure 8 compares the experimentally determined α′ phase unit cell volume and the theoretical unit cell volume predicted by thermal expansion. This comparison aims to understand the contribution of the thermal expansion towards the overall expansion of the α′ unit cell. The curve denoting the experimentally determined unit cell volume overlaps well with the one predicted by thermal expansion till 375°C. Hence, the α′ phase unit cell expansion until 375°C can be entirely attributed to the thermal expansion.

Stage 2: 375°C to 750°C: The faster α′ phase unit cell expansion during stage 2 suggests an additional factor driving the α′ phase unit cell expansion as supposed to the constant expansion rate predicted from the CTE of the α phase in ref. [27]. Additionally, the dilatometric analysis indicated a phase transformation between 450-650°C, that was later confirmed as the nucleation of the β phase based on the diffraction patterns. The overlap between the two events, viz. faster α′ unit cell expansion and β phase nucleation, must be investigated in detail. Moreover, numerous studies have shown that β phase nucleation is preceded by the formation of an intermediate hexagonal phase enriched in the β stabilizing element [28,29]. Recently, Wang et al. also discovered a thin transitionary V enriched (~ 19 wt.%) hexagonal phase at the inter-lath boundary, facilitating the α′ to α + β phase transformation [30]. The formation of the V-rich transitionary phase would cause V depletion in the bulk of neighboring α′ laths, reducing the V concentration of α′ phase to the

equilibrium V concentration of the α phase. Previous studies have demonstrated an inverse linear relationship between the V concentration and lattice parameters of α and β phases in the Ti-V system [31]. Thus, V depletion from the bulk of the α′ phase upon β nucleation could explain the accelerated expansion of the hexagonal α′ unit cell. Though simultaneous accumulation of Al in the α′ unit cell which is rejected from the newly formed β regions, should have lowered the overall expansion of the α′ unit cell on account of Al being a smaller atom than Ti [32,33]. However, the smaller size difference between Al (0.143 nm) and Ti (0.147 nm) than between V (0.134 nm) and Ti (0.147 nm) could have caused the expansion from outward V diffusion to overcompensate the shrinkage due to an increased Al concentration [34]. Finally, after sufficient V segregation at the inter-lath boundary, β phase nucleates at 575°C.

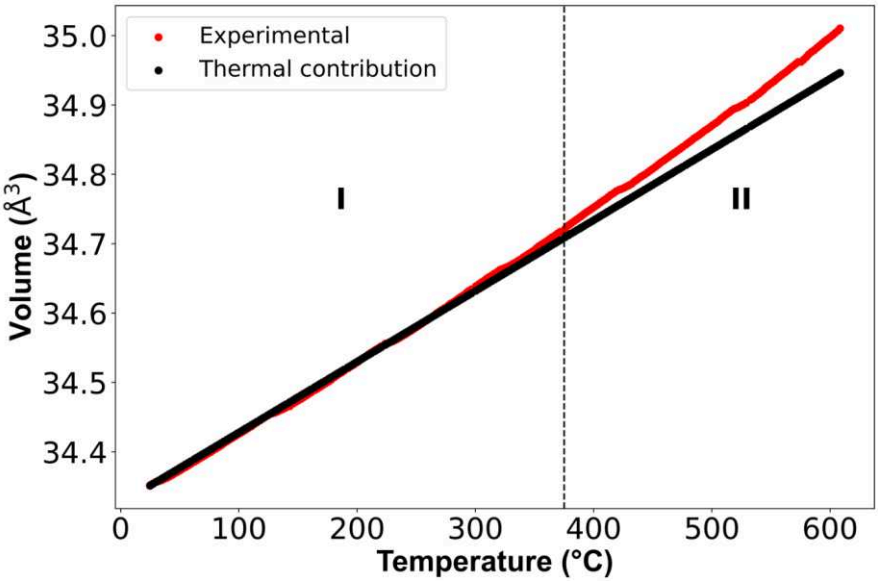

Figure 8: Evolution of the volume of the α/α' phase unit cell with temperature.

Stage 3: 750°C to 1000°C: During stage 3, after the completion of α′ decomposition, even more accelerated expansion of the α lattice was observed while the β phase lattice expansion rate slowed down. The evolution of α and β phase lattice parameters can be explained by the variation of the V concentration in α and β phases, shown in Figure 9 (A, B). Figure 9 (A) indicates a decrease in V content in the α phase from 3 mol% to 2 mol% between 750-1000°C leading to the α phase unit cell expansion. Regarding the β phase, Thermocalc simulations predicts the lowering of V concentration in the β phase from 24 mol% to 4.33 mol% in the temperature range of 750 to 1000°C. At the same time, the V depletion rate reduces beyond 750°C, as indicated by Figure 9 (B). This results in a decreasing expansion rate of the β phase unit cell (Figure 6). Surprisingly, similar evolution in β phase lattice parameter was observed for the mill-annealed Ti-6Al-4V [27].

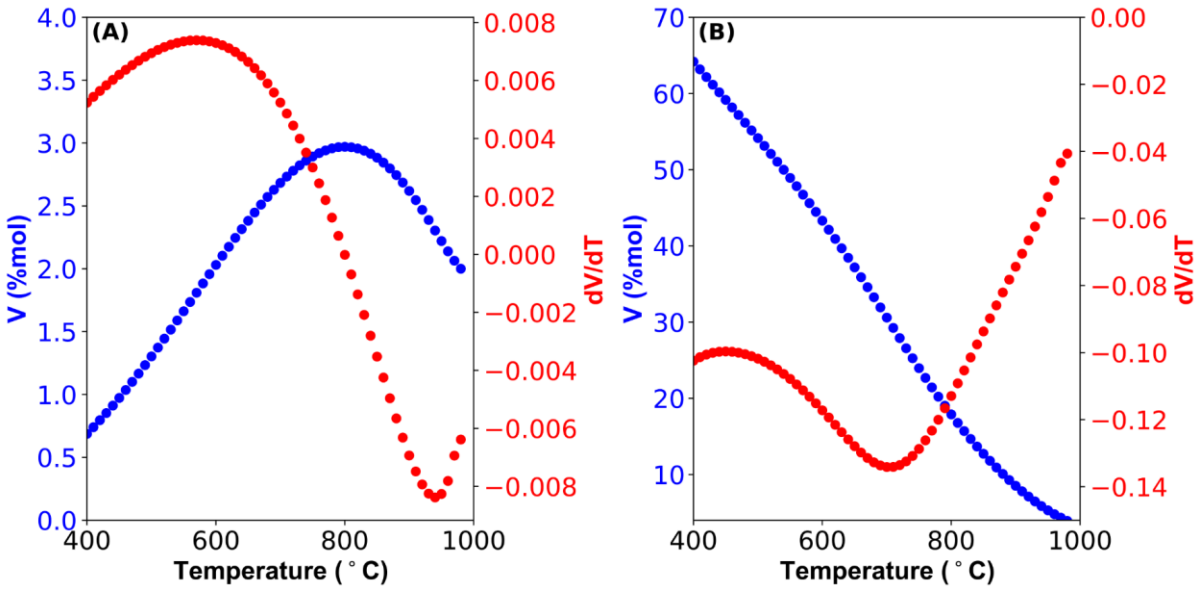

Figure 9: Evolution of the V content with temperature in (A) α phase and (B) β phase.

4.2. Stress relaxation process

Residual stress relaxation primarily occurs through the conversion of the elastic to inelastic strain, such as plastic deformation and creep. Wang et al. suggested dislocation climb and glide as the primary stress relaxation mechanism for L-PBF processed Ti-6Al-4V [35]. So, stress relaxation can only occur when the stored elastic energy (residual stresses) is utilized in mobilizing the dislocations, the source of inelastic strain. Thermodynamically, dislocation mobilization occurs when the total driving comprising of the stored elastic energy (residual stresses, ΔW) and thermal activation energy (ΔG) surpasses a certain threshold barrier energy (F), which is temperature independent [36].

$$\Delta W + \Delta G > F \tag{1}$$

In the present study, significant stress relaxation is not observed below 450°C, indicating that the stored elastic energy cannot be converted into inelastic strain below 450°C. This can be attributed to the combination of relatively smaller ΔG term below 450°C and insufficient stored elastic energy, which fails to activate dislocation motion. Furthermore, the FWHM of the α′ reflections remains unchanged until 450°C, suggesting minimal change in the dislocation density. Stress relaxation is observed only above 450°C, suggesting the conversion of the stored elastic energy into plastic deformation. This can be attributed to the increased contribution from the ΔG term which helps to surpass the threshold energy barrier, facilitating the dislocation motion. Thus, the stored elastic energy gets converted into plastic deformation, and residual stress drops. Additionally, a precipitous drop in FWHM of the α′ reflection above 450°C can be linked to decreased dislocation density, due to dislocation annihilation facilitated by the activation of the dislocation climb mechanism. Finally, a stress-free state is obtained at around 750°C. A similar phenomenon is also confirmed for another titanium alloy [37].

Figure 10 summaries the overall stress-relaxation and the solid-state phase transformation events occurring during the heating.

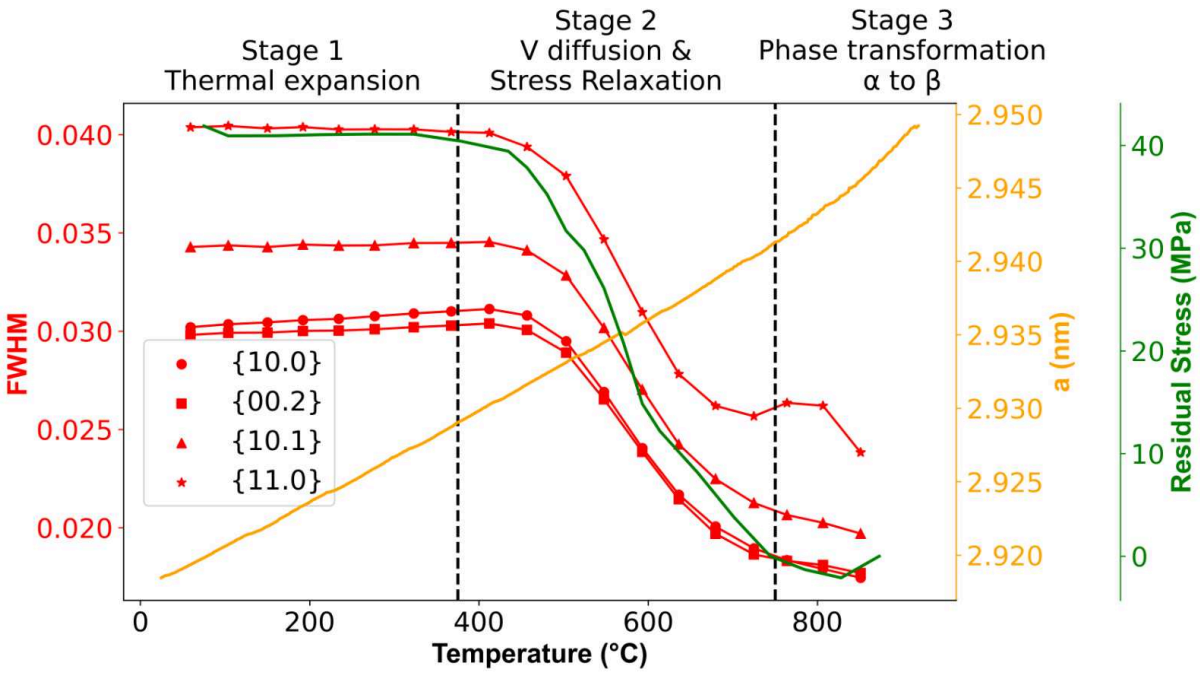

Figure 10: Summary of the martensite decomposition and the stress relaxation process.

4.3. Influence of starting microstructure on the evolution of lattice parameter

The current paragraph links the thermal expansion of the hexagonal unit cell with the initial microstructure. Until now, most studies have focused either solely on L-PBF [20] or conventionally produced Ti-6Al-4V [27,38]. In a conventionally produced α+β microstructure, Elmer et al. reported a drop in the thermal expansion rate for the α phase between 500-750°C [27]. On the other hand, Lakroune et al. reported a monotonously increasing thermal expansion rate for the α′ phase unit cell, supporting the thermal evolution trend observed in the current investigation [20]. Brown et al. compared and reported a difference in the thermal evolution of the hexagonal unit cell parameters for L-PBF and conventionally processed Ti-6Al-4V [19]. The same authors reported a uniform expansion rate for conventionally produced Ti-6Al-4V and a monotonously increasing thermal expansion rate for the L-PBF processed Ti-6Al-4V, similar to the present study. They, however, did not report a declinein the thermal expansion rate for the α phase in the conventionally produced Ti-6Al-4V, opposed to Elmer et al. It should be noted that Brown et al. reported only the interplanar spacing for the {10.0} and {10.2} directions and not the actual unit cell parameters [19,27]. Thus, there is no clear link between the initial microstructure and thermal expansion behavior.

Here, the thermal expansion behavior of the conventionally produced α+β microstructure, reported by Elmer et al., is compared with the thermal expansion of the α′ phase. As observed in Figure 5 (A, B), when the initial Ti-6Al-4V is purely composed of the α′ phase, the expansion rate of the α′ phase unit cell along the a- and c-direction increases in three distinct stages during heating from 25 to 1000°C. Contrary to the α′ phase, a different unit cell parameter evolution is observed for the α phase in a conventionally produced and mill-annealed Ti-6Al-4V part with an α + β microstructure (indicated in Figure 11) [27]. In Figure 11, Elmer et al. reported a constant expansion rate for the α phase along the a-direction until 550°C. After that, the expansion rate drops slightly between 550-750°C, followed by an increased expansion rate from 750°C to the β transus temperature. The different evolution of the expansion rate for the L-PBF process induced α′ phase and the α phase in mill-annealed α+β microstructures could be attributed to the different chemical composition evolution during heating in α and α′ phases. For the equilibrium α+β microstructure, the α phase unit cell expansion until 550°C is

primarily fueled by the thermal expansion that overcompensates any possible unit cell contraction due to an increasing V content, as predicted by Thermocalc (Figure 9 (A)). However, the unit cell expansion slows down between 550-700°C due to an increased rate of V influx in the same temperature range (Figure 9 (A)). After reaching the peak V concentration at 750°C, V concentration decreases, which again drives the α phase unit cell expansion till the beta transus temperature.

On the other hand, the hexagonal unit cell of α′ is already supersaturated with V due to the high cooling rates resulting from the L-PBF process [16]. Upon heating, V diffuses outward due to a high thermodynamic driving force [38]. The V expulsion rate increases with temperature resulting in the hexagonal unit cell expansion at an increasingly faster rate. Thus, the V content in α′ martensite does not follow the same trend as in the equilibrium α phase. As a result, a different unit cell parameter evolution is observed during the heating of martensite. On the other hand, the β phase lattice parameter shows a similar trend as that reported by Elmer et al. because the chemical composition of β evolved similarly in both cases.

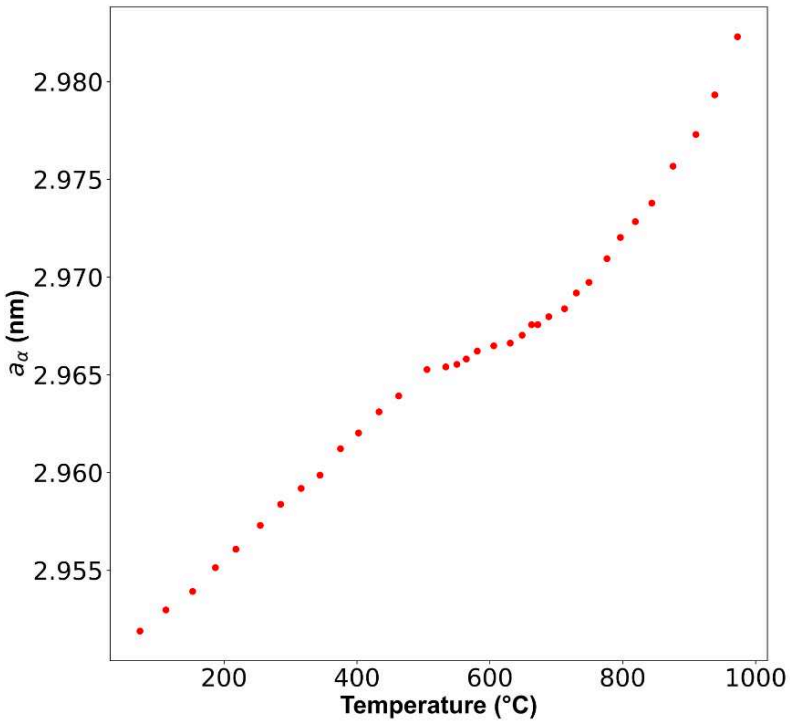

Figure 11: Thermal evolution of the a lattice parameter of α phase in the mill-annealed Ti-6Al-4V as reported by Elmer et al. [27]

5. Summary

In-situ synchrotron high energy X-ray diffraction (HEXRD) and dilatometry were employed to study the phase transformations and the stress relaxation process in laser powder bed fusion (L-PBF) processed Ti-6Al-4V during continuous heating.

- Dilatometric analysis revealed two phase transformations: the nucleation of β phase in the temperature range of 450-650°C and the α-to-β phase transformation between 750-1000°C.

- Detailed investigation with HEXRD revealed three different stages in the expansion behavior of the α/α′ phase unit cell.

- During the first stage (RT to 375°C), thermal expansion primarily drove the α′ unit cell expansion.
- The enhanced α′ phase unit cell expansion during the second stage (400 to 700°C) was attributed to the outward V diffusion that eventually led to the nucleation of the β phase at 575°C. Besides a non-linear thermal evolution of the α′ phase unit cell dimensions during this second stage, the macroscopic and microscopic residual stress in the α phase, as monitored by the deviatoric stress component and FWHM, decreased significantly between 450 and 750°C.
- Complete relaxation of L-PBF-induced residual stress was observed at the onset of stage 3 (750 to 1000°C). Additionally, complete martensite decomposition was achieved at around 750-800°C, and later, the allotropic α-to-β solid-state phase transformation picks up above 750°C. In stage 3, the α phase unit cell expanded even more rapidly because of the increased V expulsion rate at temperature above 750°C, whereas the lower rate of the β phase unit cell expansion was due to the decreased rate of V expulsion.

- A different unit cell expansion behavior was observed between the hexagonal α′ and α phases in LPBF and conventionally processed Ti-6Al-4V, driven by a compositional difference between both phases. The ever-increasing expansion rate of the V supersaturated α′ phase unit cell in L-PBF processed Ti-6Al-4V was fueled by a combination of thermal expansion and continuous V rejection. Contrary to the ever-increasing thermal expansion rate of the L-PBF α′ phase, the expansion rate of the hexagonal α phase in conventionally processed Ti-6Al-4V decreases between 550-750°C due to slowed V rejection.

Acknowledgements

The work leading to this publication has been funded by the ICON project “PROCSIMA”, which fits in the MacroModelMat (M3) research program, coordinated by Siemens (Siemens Digital Industries Software, Belgium) and funded by SIM (Strategic Initiative Materials in Flanders) and VLAIO (Flemish government agency Flanders Innovation & Entrepreneurship).

We acknowledge DESY (Hamburg, Germany), a member of the Helmholtz Association HGF, for the provision of experimental facilities. Parts of this research were carried out at PETRA III and we would like to thank Dr. Andreas Stark, Dr. Emad Maawad and Dr. Norbert Schell for assistance in using beamline P07 and the in-situ dilatometer. Beamtime was allocated for proposal I-20190769 EC. This work has further benefitted from support by the project CALIPSOplus [Grant Agreement 730872] from the EU Framework Programme for Research and Innovation HORIZON 2020.

Data Availability

The raw/processed data required to reproduce these findings cannot be shared at this time as the data also forms part of an ongoing study.

References:

[1] S. Dinkar JADHAV, Laser-Based Powder Bed Fusion Additive Manufacturing of Highly Conductive Copper and Copper Alloys, (2021).

[2] T. Pereira, J. V. Kennedy, J. Potgieter, A comparison of traditional manufacturing vs additive manufacturing, the best method for the job, Procedia Manuf. 30 (2019) 11–18. https://doi.org/10.1016/j.promfg.2019.02.003.

[3] L. Thijs, Microstructure and texture of metal parts produced by Selective Laser Melting, KU

Leuven, 2014.

[4] T. Ahmed, H.J. Rack, Phase transformations during cooling in α + β titanium alloys, Mater. Sci. Eng. A. 243 (1998) 206–211. https://doi.org/10.1016/s0921-5093(97)00802-2.

[5] G.M. Ter Haar, T.H. Becker, Laser powder bed fusion produced Ti-6Al-4V: Influence of high-energy process parameters on in-situ martensite decomposition and prior beta grain texture, J. Alloys Compd. 918 (2022) 165497. https://doi.org/10.1016/j.jallcom.2022.165497.

[6] W. Xu, M. Brandt, S. Sun, J. Elambasseril, Q. Liu, K. Latham, K. Xia, M. Qian, Additive manufacturing of strong and ductile Ti-6Al-4V by selective laser melting via in situ martensite decomposition, Acta Mater. 85 (2015) 74–84. https://doi.org/10.1016/j.actamat.2014.11.028.

[7] W. Xu, M. Brandt, S. Sun, J. Elambasseril, Q. Liu, K. Latham, K. Xia, M. Qian, Additive manufacturing of strong and ductile Ti – 6Al – 4V by selective laser melting via in situ martensite decomposition, Acta Mater. 85 (2015) 74–84. https://doi.org/10.1016/j.actamat.2014.11.028.

[8] H. Ali, L. Ma, H. Ghadbeigi, K. Mumtaz, In-situ residual stress reduction , martensitic decomposition and mechanical properties enhancement through high temperature powder bed pre-heating of Selective Laser Melted Ti6Al4V, Mater. Sci. Eng. A. 695 (2017) 211–220. https://doi.org/10.1016/j.msea.2017.04.033.

[9] W. Xu, E.W. Lui, A. Pateras, M. Qian, M. Brandt, In situ tailoring microstructure in additively manufactured Ti-6Al-4V for superior mechanical performance, Acta Mater. 125 (2017) 390–400. https://doi.org/10.1016/j.actamat.2016.12.027.

[10] B. Vrancken, S. Buls, J.-P. Kruth, J. Van Humbeeck, Influence of preheating and oxygen content on Selective Laser Melting of Ti6Al4V, Proc. 16th RAPDASA Conf. (2015). uhttps://lirias.kuleuven.be/retrieve/385993DFull%0Apaper%0A[freely%0Aavailable].

[11] D. Kouprianoff, W. Preez, Reducing time and cost of the heat treatment post-processing of additively manufactured Ti6Al4V, Mater. Today Commun. 35 (2023) 106186. https://doi.org/10.1016/j.mtcomm.2023.106186.

[12] M.T. Tsai, Y.W. Chen, C.Y. Chao, J.S.C. Jang, C.C. Tsai, Y.L. Su, C.N. Kuo, Heat-treatment effects on mechanical properties and microstructure evolution of Ti-6Al-4V alloy fabricated by laser powder bed fusion, J. Alloys Compd. 816 (2020) 152615. https://doi.org/10.1016/j.jallcom.2019.152615.

[13] M. Frkan, R. Konecna, G. Nicoletto, L. Kunz, Microstructure and fatigue performance of SLM-fabricated Ti6Al4V alloy after different stress-relief heat treatments, Transp. Res. Procedia. 40 (2019) 24–29. https://doi.org/10.1016/j.trpro.2019.07.005.

[14] G.M. Ter Haar, T.H. Becker, Low temperature stress relief and martensitic decomposition in selective laser melting produced Ti6Al4V, Mater. Des. Process. Commun. 3 (2021) 2–7. https://doi.org/10.1002/mdp2.138.

[15] X. Tan, Y. Kok, W.Q. Toh, Y.J. Tan, M. Descoins, D. Mangelinck, S.B. Tor, K.F. Leong, C.K. Chua, Revealing martensitic transformation and α/β interface evolution in electron beam melting three-dimensional-printed Ti-6Al-4V, Sci. Rep. 6 (2016) 1–10. https://doi.org/10.1038/srep26039.

[16] F.R. Kaschel, R.K. Vijayaraghavan, A. Shmeliov, E.K. McCarthy, M. Canavan, P.J. McNally, D.P. Dowling, V. Nicolosi, M. Celikin, Mechanism of stress relaxation and phase transformation in additively manufactured Ti-6Al-4V via in situ high temperature XRD and TEM analyses, Acta Mater. 188 (2020) 720–732. https://doi.org/10.1016/j.actamat.2020.02.056.

[17] A. Umapathi, S. Swaroop, Measurement of residual stresses in titanium alloys using

synchrotron radiation, Meas. J. Int. Meas. Confed. 140 (2019) 518–525. https://doi.org/10.1016/j.measurement.2019.04.021.

[18] No Title, (n.d.). http://www.datech-scientific.co.uk/analysis/xrd/ (accessed September 24, 2023).

[19] D.W. Brown, V. Anghel, L. Balogh, B. Clausen, N.S. Johnson, R.M. Martinez, D.C. Pagan, G. Rafailov, L. Ravkov, M. Strantza, E. Zepeda-Alarcon, Evolution of the Microstructure of Laser Powder Bed Fusion Ti-6Al-4V During Post-Build Heat Treatment, Metall. Mater. Trans. A Phys. Metall. Mater. Sci. 52 (2021) 5165–5181. https://doi.org/10.1007/s11661-021-06455-7.

[20] Y. Lakroune, D. Connétable, J. Hugues, P. Hermantier, P. Barriobero-Vila, M. Dehmas, Microstructural evolution during post heat treatment of the Ti–6Al–4V alloy manufactured by laser powder bed fusion, J. Mater. Res. Technol. 23 (2023) 1980–1994. https://doi.org/10.1016/j.jmrt.2023.01.123.

[21] A.P. Hammersley, FIT2D: A multi-purpose data reduction, analysis and visualization program, J. Appl. Crystallogr. 49 (2016) 646–652. https://doi.org/10.1107/S1600576716000455.

[22] MAUD, (n.d.). http://maud.radiographema.com/ (accessed November 14, 2022).

[23] T.H. de Keijser, J.I. Langford, E.J. Mittemeijer, A.B.P. Vogels, Use of the Voigt function in a single-line method for the analysis of X-ray diffraction line broadening, J. Appl. Crystallogr. 15 (1982) 308–314. https://doi.org/10.1107/s0021889882012035.

[24] L. Lutterotti, D. Chateigner, S. Ferrari, J. Ricote, Texture, residual stress and structural analysis of thin films using a combined X-ray analysis, Thin Solid Films. 450 (2004) 34–41. https://doi.org/10.1016/j.tsf.2003.10.150.

[25] M. Gushchina, G. Turichin, O. Klimova-Korsmik, K. Babkin, L. Maggeramova, Features of heat treatment the ti-6al-4v gtd blades manufactured by dld additive technology, Materials (Basel). 14 (2021). https://doi.org/10.3390/ma14154159.

[26] Z.Y. Zhong, H.G. Brokmeier, W.M. Gan, E. Maawad, B. Schwebke, N. Schell, Dislocation density evolution of AA 7020-T6 investigated by in-situ synchrotron diffraction under tensile load, Mater. Charact. 108 (2015) 124–131. https://doi.org/10.1016/j.matchar.2015.09.004.

[27] J.W. Elmer, T.A. Palmer, S.S. Babu, E.D. Specht, In situ observations of lattice expansion and transformation rates of α and β phases in Ti-6Al-4V, Mater. Sci. Eng. A. 391 (2005) 104–113. https://doi.org/10.1016/j.msea.2004.08.084.

[28] C. Liu, X. Hu, L. Qi, H. Chen, Z. Li, X. Zhang, H. Yan, K. Zhou, M. Song, Y. Wang, J.F. Nie, Unusual precipitation induced by solute segregation in coherent twin boundary in titanium alloys, Acta Mater. 242 (2023) 118466. https://doi.org/10.1016/j.actamat.2022.118466.

[29] X. Fu, X.D. Wang, B. Zhao, Q. Zhang, S. Sun, J.J. Wang, W. Zhang, L. Gu, Y. Zhang, W.Z. Zhang, W. Wen, Z. Zhang, L. qing Chen, Q. Yu, E. Ma, Atomic-scale observation of non-classical nucleation-mediated phase transformation in a titanium alloy, Nat. Mater. 21 (2022) 290–296. https://doi.org/10.1038/s41563-021-01144-7.

[30] H. Wang, Q. Chao, H.S. Chen, Z.B. Chen, S. Primig, W. Xu, S.P. Ringer, X.Z. Liao, Formation of a transition V-rich structure during the α′ to α + β phase transformation process in additively manufactured Ti-6Al-4 V, Acta Mater. 235 (2022). https://doi.org/10.1016/j.actamat.2022.118104.

[31] W. Mei, J. Sun, Y. Wen, A first-principles study of displacive β to ω transition in Ti-V alloys, Prog. Nat. Sci. Mater. Int. 27 (2017) 703–708. https://doi.org/10.1016/j.pnsc.2017.10.003.

[32] V.I. Fadeeva, A. V. Leonov, E. Szewczak, H. Matyja, Structural defects and thermal stability

of Ti(Al) solid solution obtained by mechanical alloying, Mater. Sci. Eng. A. 242 (1998) 230–234. https://doi.org/10.1016/s0921-5093(97)00503-0.

[33] O.B. Perevalova, E. V. Konovalova, N.A. Koneva, Effect of Aluminum Concentration on the Lattice Parameters and Mean-Square Displacements of Atoms in Cu–Al and Ti–6Al–4V Alloys, Bull. Russ. Acad. Sci. Phys. 83 (2019) 693–696. https://doi.org/10.3103/S1062873819060236.

[34] J.C. Slater, Atomic radii in crystals, J. Chem. Phys. 41 (1964) 3199–3204. https://doi.org/10.1063/1.1725697.

[35] Z. Wang, A.D. Stoica, D. Ma, A.M. Beese, Stress relaxation behavior and mechanisms in Ti-6Al-4V determined via in situ neutron diffraction: Application to additive manufacturing, Mater. Sci. Eng. A. 707 (2017) 585–592. https://doi.org/10.1016/j.msea.2017.09.071.

[36] H. Song, H. Gao, Q. Wu, Y. Zhang, Effects of segmented thermal-vibration stress relief process on residual stresses, mechanical properties and microstructures of large 2219 Al alloy rings, J. Alloys Compd. 886 (2021) 161269. https://doi.org/10.1016/j.jallcom.2021.161269.

[37] I. V. Ivanov, K.I. Emurlaev, D. V. Lazurenko, A. Stark, I.A. Bataev, Rearrangements of dislocations during continuous heating of deformed β-TiNb alloy observed by in-situ synchrotron X-ray diffraction, Mater. Charact. 166 (2020) 110403. https://doi.org/10.1016/j.matchar.2020.110403.

[38] G. Lindwall, K.W. Moon, Z. Chen, M. Mengason, M.E. Williams, J.M. Gorham, J.C. Zhao, C.E. Campbell, Diffusion in the Ti-Al-V System, J. Phase Equilibria Diffus. 39 (2018) 731–746. https://doi.org/10.1007/s11669-018-0673-9.

[39] H.R. Wenk, L. Lutterotti, P. Kaercher, W. Kanitpanyacharoen, L. Miyagi, R. Vasin, Rietveld texture analysis from synchrotron diffraction images. II. Complex multiphase materials and diamond anvil cell experiments, Powder Diffr. 29 (2014) 220–232. https://doi.org/10.1017/S0885715614000360.

Appendix A

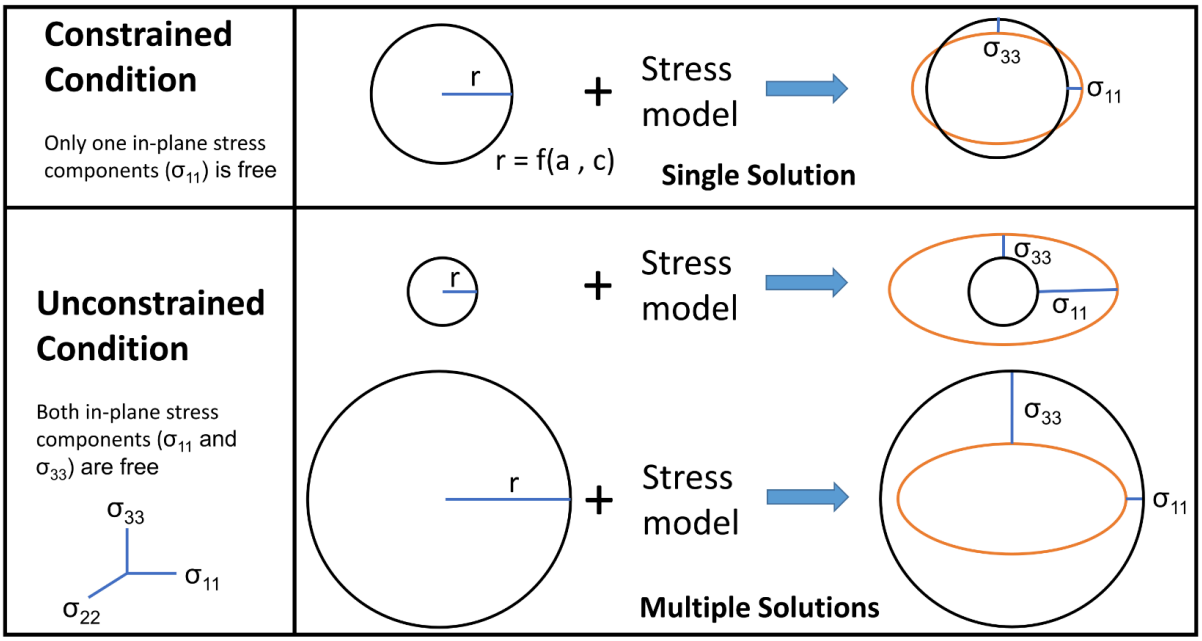

Figure A1: Difference between the Rietveld refinement of diffraction rings with a constrained and an unconstrained deviatoric stress model. Orange coloured ellipses represent the experimental 2D diffraction ring. The ellipticity of the diffraction ring is exaggerated for the illustration purpose.

Figure A1 summarizes the difference between Rietveld refinements of diffraction rings performed with a constrained ($\sigma_{11} = -\sigma_{33}$) and an unconstrained ($\sigma_{11}$ and σ_{33} are not related) deviatoric stress model. The unconstrained stress model can result in multiple solutions, meaning a good fit between the experimental and calculated diffraction pattern can be obtained for different combinations of the lattice parameters (a, c) and in-plane stress components (σ_{11} & σ_{33}). Two of such instances are showcased in Figure A1. The first instance shows a case where the combination of a small circle (corresponding to large lattice parameters) with in-plane compressive stresses as $|\sigma_{11}| > |\sigma_{33}|$ can fit the experimental diffraction ring. Similarly, a large circle (corresponding to small lattice parameters) with a different tensile in-plane stress combination, i.e., $\sigma_{33} > \sigma_{11}$, can fit the same diffraction ring. Thus, a unique solution cannot be achieved by the unconstrained model. On the other hand, Rietveld refinement with the constrained stress model leads to a unique solution.

Appendix B

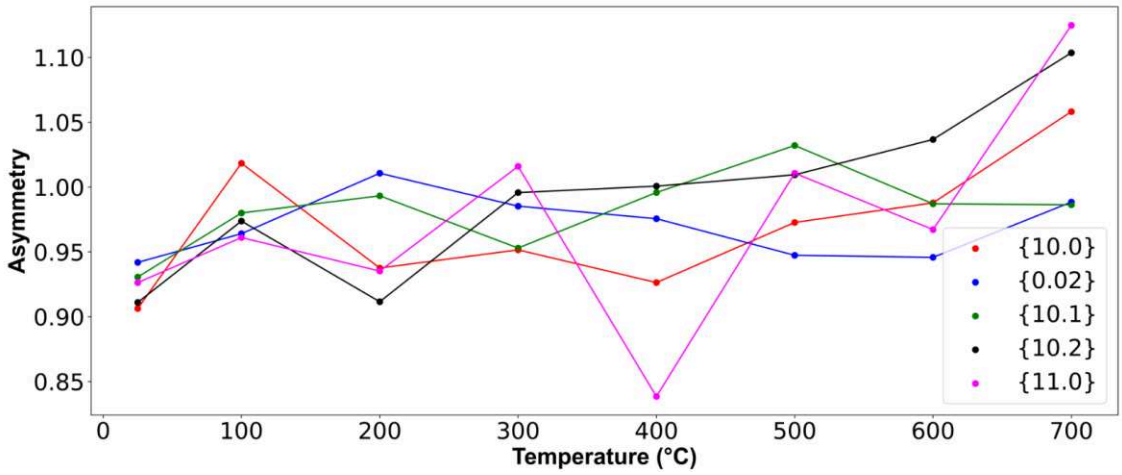

Figure B1: Asymmetry of three α/α' reflections as function of temperature in an azimuthal range of 10.° centred around the horizontal direction of the detector.

Figure B1 presents the evolution with temperature of the peak asymmetry of the {10.0}, {10.1} and {10.2} peaks of the α phase. Here, the degree of asymmetry is defined by the ratio of the FWHMs for left and for right sides of a fitted split pseudo Voigt function. No clear trend could be observed in the evolution of the asymmetry.

Appendix C

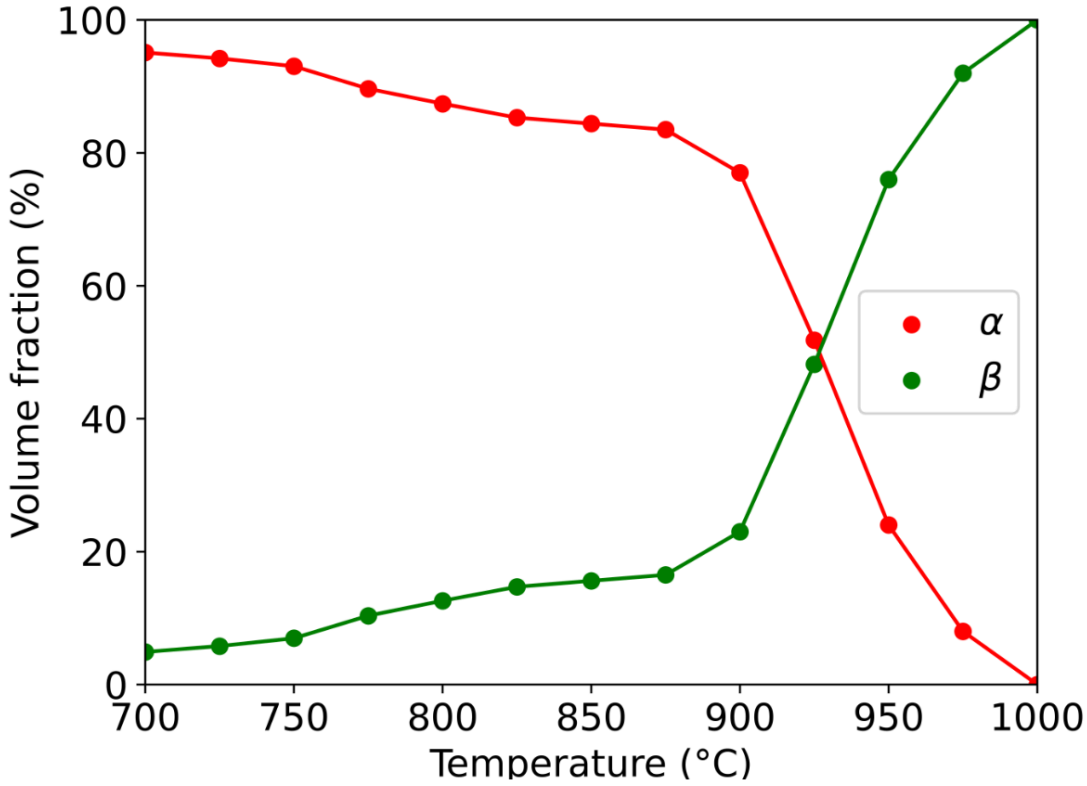

Figure C1: Evolution of the phase fractions with temperature determined via Rietveld refinement of the complete 2D diffraction patterns.

Appendix D

Figure D1 highlights the motivation behind choosing the deviatoric stress component as the representative quantity for the residual stress state. Figure D1 displays a 2D diffraction pattern in stress-free condition unrolled along the azimuth. Due to the absence of deviatoric stress, the peak positions remain constant across all azimuths. Under the application of external hydrostatic tensile stress, each peak shifts to lower diffraction angles uniformly across all azimuths, as indicated in Figure 9 (B). A similar peak shift independent of azimuth can also occur due to thermal expansion or changing chemical composition. Thus, the presence of these two factors (thermal expansion and varying chemical composition) complicates the calculation of the hydrostatic component of the residual stress. However, under the combined influence of hydrostatic and deviatoric stress, peak positions are no longer constant across the whole azimuthal range [39]. This translates into an elliptical 2D diffraction ring, which can be fitted by incorporating an appropriate strain (or stress) model during the Rietveld refinement (see Appendix A). Tracking the deviatoric component of the residual stress is possible because chemical composition changes do not produce deviatoric stresses in the material. On the other hand, thermal expansion can affect the deviatoric stresses in a textured sample due to different CTE along the a- and c-axis. This possibility was taken into account and E-WIMV model was used to model crystallographic texture. Hence, the deviatoric stresses are free of thermal expansion and compositional changes.

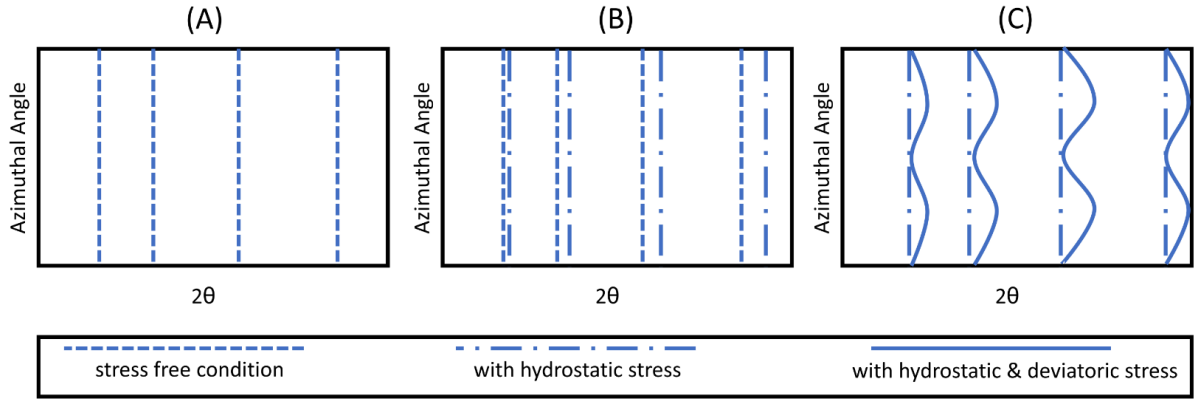

Figure D1: Hypothetical diffraction patterns plotted as azimuthal angle vs 2θ under the (A) stress-free condition, (B) influence of hydrostatic stress and (C) combined influence of hydrostatic & deviatoric stressα